AN ATTEMPT TO MODEL SHRINKAGE CAVITY COUPLED WITH MACROSEGREGATION IN STEEL INGOTS

M. Wu[1,2*], A. Ludwig[2], A. Kharicha[1,2]

[1] Christian Doppler Laboratory for Advanced Process Simulation of Solidification and Melting, Montanuniversitaet Leoben, Austria
[2] Chair of Simulation and Modelling of Metallurgical Processes, Montanuniversitaet Leoben, Austria
[*] Corresponding author: menghuai.wu@unileoben.ac.at

ABSTRACT

This work is to extend an existing 3-phase mixed columnar-equiaxed solidification model to treat the formation of shrinkage cavity by including an additional phase. In the previous model a mixed columnar and equiaxed solidification approach that considers the multiphase transport phenomena (mass, momentum, species and enthalpy) is proposed to calculate the as-cast structure including columnar-to-equiaxed transition (CET) and formation of macrosegregation. In order to incorporate the formation of shrinkage cavity, a supplementary phase, i.e. gas phase or covering liquid slag phase, is considered in addition to the previously introduced 3 phases (parent melt, solidifying columnar dendrite trunks and equiaxed grains). No mass and species transfer between the new phase and the other 3 phases is necessary, but momentum and energy transfer is of critical importance for the formation of the shrinkage cavity and with that the flow and formation of macrosegregation would be influenced. Some modelling approaches for the momentum and energy transfer are suggested and tested.

KEYWORDS

steel, ingot, macrosegregation, shrinkage, cavity, porosity

INTRODUCTION

Typical steel ingots solidify with a shrinkage cavity at the hot top, and microscopic shrinkage porosity and macrosegregation located somewhere in the cross section [1]. Those undesired casting defects result from the volume change during solidification (and the resulting feeding flow), thermal-solutal convection and crystal sedimentation. The formation mechanisms of these phenomena are rather complex as they interact with each other. Scientists have tried different approaches to model or predict their occurrence [2-9], but no model is available to calculate, in a coupled manner, shrinkage cavity/porosity together with macrosegregation of the art as shown in Fig. 1. The formation process of the above defects is multiphasic in nature.

This work is to extend an existing 3-phase mixed columnar-equiaxed solidification model [10] to treat the formation of shrinkage cavity by including an additional gas (or covering slag) phase [11]. Four phases are necessarily considered: primary liquid melt, equiaxed crystals, col-

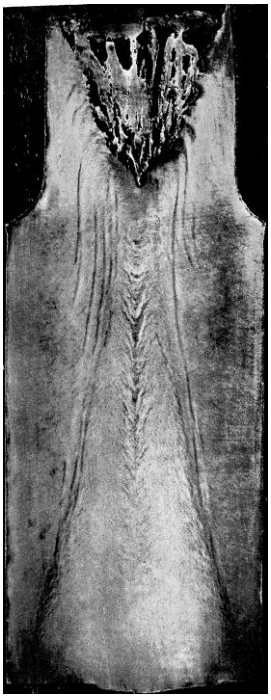

Figure 1. Example of a shrinkage cavity and macrosegregation (sulphur print) in a steel ingot (reproduced from literature [1]).

INDEX

umnar dendrite trunks, and gas. The final goal is to develop an Eulerian multiphase solidification model at the process scale to calculate the as-cast columnar-equiaxed structure including CET (columnar-to-equiaxed transition), shrinkage cavity/porosity, and macrosegregation for industrial castings.

1. THE NUMERICAL MODEL

1.1 Brief model description

- Phase definition: primary liquid (ℓ), solidifying equiaxed phase (e), columnar phase (c), and gas phase (g). Their volume fractions (f_ℓ, f_e, f_c, f_g) sum up to one. The volume averaged mass transport equations considering the mass transfer due to solidification are solved.
- There is no mass transfer between the gas and the other phases, and the gas phase is supposed to be immiscible with the other metal phases. In fact, the gas phase is sucked into the casting domain to feed the shrinkage cavity. The interface between the gas and the other phases is explicitly solved. The microscopic porosity that forms deep in the interdendritic region is treated differently (Section 2.3).
- The liquid, equiaxed and gas phases are moving phases, for which the corresponding volume averaged Navier-Stokes equations are solved to get $\vec{u}_\ell$, $\vec{u}_e$ and $\vec{u}_g$. For the columnar phase we assume $\vec{u}_c \equiv 0$.
- Enthalpy equations for all 4 phases are solved. Due to the fact of relatively large thermal diffusivity, we assume that only one temperature (T) represents each volume element. Therefore, a large inter-phasic volume heat exchange coefficient is applied to balance the temperatures among the phases.
- Three volume-averaged concentration fields (c_ℓ, c_e, c_c) are solved for the three metal phases. Thermodynamic equilibrium condition is assumed to apply at the liquid-solid interface, and corresponding solute partitioning at the interface occurs during solidification.
- A diffusion-governed growth kinetic is considered to calculate the growth of crystals.
- Ideal morphologies for both solid phases are assumed: spheres for equiaxed (globular) grains and cylinders for columnar (cellular) dendrite trunks.
- The columnar dendrite trunks are assumed to be originated from the mould wall. Neither nucleation of columnar trunks nor equiaxed-to-columnar transition (ECT) is taken into account.
- Heterogeneous nucleation and transport of the equiaxed crystals are considered. Grain fragments brought into the mould during filling, further fragmentation of dendrites during solidification and the attachment of equiaxed grains into columnar area (as a part of the columnar phase) are ignored.
- The diameter, d_e, and number density, n_e, of equiaxed grains and the diameter, d_c, of the columnar trunks are explicitly calculated, while a constant value for the primary arm spacing of columnar dendrites, λ_1, is assumed.

Details of the three-phase mixed columnar-equiaxed solidification model were described elsewhere [10]. Treatment of the gas phase, the formation of the shrinkage cavity and of porosity is described below.

1.2 Treatment of interactions between gas and other phases

As no mass/species transfer between the gas and the other metal phases is considered, only enthalpy and momentum conservation equations for the gas phase are necessarily solved:

$$\frac{\partial}{\partial t}\left(f_g \rho_g h_g\right) + \nabla \cdot \left(f_g \rho_g \vec{u}_g h_g\right) = \nabla \cdot (f_g k_g \nabla \cdot T_g) + Q_{\ell g}^{ex} + Q_{eg}^{ex} + Q_{cg}^{ex} \qquad (1)$$

$$\frac{\partial}{\partial t}\left(f_g \rho_g \vec{u}_g\right) + \nabla \cdot \left(f_g \rho_g \vec{u}_g \otimes \vec{u}_g\right) = -f_g \nabla p + \nabla \cdot \bar{\bar{\tau}}_g + f_g \rho_g \vec{g} + \vec{U}_{\ell g}^{ex} + \vec{U}_{eg}^{ex} + \vec{U}_{cg}^{ex} \qquad (2)$$

Key feature by introducing a new gas phase in the mixed columnar-equiaxed solidification is to treat the exchange terms, which are superscripted with 'ex' in Eq. (1) and (2). They are summarized in Table 1.

INDEX

Table 1. Momentum and energy exchange terms between gas and other metal phases

<table>
<tr><td>$Q_{\ell g}^{ex} = H_{\ell g}^{*} f_{\ell} f_{g} (T_{\ell} - T_{g})$
$Q_{eg}^{ex} = H_{eg}^{*} f_{e} f_{g} (T_{e} - T_{g})$
$Q_{cg}^{ex} = H_{cg}^{*} f_{c} f_{g} (T_{c} - T_{g})$</td><td colspan="2">$H_{\ell g}^{*}$ [W/m^3/K]: the volume heat exchange coefficient is modelled according to Ranz-Marshall [11,12].
H_{eg}^{*} and H_{cg}^{*} : a constant volume heat exchange coefficient of 500 W/m^3/K is assumed.</td></tr>
<tr><td>$\vec{U}_{\ell g}^{ex} = K_{\ell g} \cdot (\vec{u}_{\ell} - \vec{u}_{g})$
$\vec{U}_{eg}^{ex} = K_{eg} \cdot (\vec{u}_{e} - \vec{u}_{g})$
$\vec{U}_{cg}^{ex} = K_{cg} \cdot (\vec{u}_{c} - \vec{u}_{g})$</td><td>$K_{pg} = \dfrac{\rho_{pg} \mathrm{Re} C_D}{144 \tau_{pg}} d_{pg} A_{pg}$
The symmetric model taken from [13] with minor modifications is applied. Subscript ‘p’ indicates different metal phases: ‘ ℓ ’, ‘e’ or ‘c’.</td><td>$\mathrm{Re} = \rho_{pg} \lvert \vec{u}_{p} - \vec{u}_{g} \rvert d_{pg} / \mu_{pg}$
$C_D = \begin{cases} 27.6 & \mathrm{Re} \le 1 \\ 24(1 + 0.15\mathrm{Re}^{0.687})/\mathrm{Re} & 1 < \mathrm{Re} \le 10^3 \\ 0.44 & \mathrm{Re} > 10^3 \end{cases}$
$\tau_{pg} = \rho_{pg} d_{pg}^2 / 18 \mu_{pg}$
$A_{pg} = 6 f_{p} f_{g} / d_{pg}$
$\mu_{pg} = \min(\mu_{p}, \mu_{g})$; $\rho_{pg} = \min(\rho_{p}, \rho_{g})$;
d_{pg} : modelling parameter (diameters) as function of volume fractions of involving phases.</td></tr>
</table>

1.3 Simplified microscopic shrinkage porosity model

The Niyama criterion modified by Carlson and Beckermann [2, 3] is implemented. We name it as CBN (Carlson-Beckermann-Niyama) criterion, Eq. (3).

$$\mathrm{CBN} = C_{\lambda} \frac{G}{\dot{T}^{5/6}} \sqrt{\frac{\Delta P_{cr}}{\mu_{\ell} \beta (T_{Liq} - T_{Eut})}} \qquad (3)$$

where C_{λ} = 1.44x10^{-4} m$\cdot$(K/s)$^{1/3}$ is a material constant being used for determining the secondary dendrite arm spacing; G and $\dot{T}$ are the temperature gradient and cooling rate, which are evaluated at a critical temperature of T_{cr} (= 0.1 $T_{Liq} + 0.9 T_{Eut}$), assuming that T_{Eut} corresponds to the end solidification; $\beta = (\rho_{s} - \rho_{\ell})/\rho_{\ell}$ is the solidification shrinkage; ΔP_{cr} is the critical pressure drop when a pore-nucleus with critical radius of r_c deep in the mushy zone can overcome capillary force ($2\sigma/r_c$) and metastatic pressure (P_{static}) to grow. ΔP_{cr} is taken as 1.01x10^5 Pa for steel [3]. The possible occurrence of shrinkage porosity and the amount of pores (volume fraction of voids) decrease with the local CBN value. The smaller the CBN value, the more probable shrinkage porosity would occur, and the larger amount of pores might form. As no threshold of CBN for the occurrence of pores can be determined in advance, this criterion is used only for qualitative evaluation of the possible occurrence of microscopic shrinkage porosity.

Although the current model offers the possibility to calculate the interdendritic flow, it is time consuming to solve the feeding deep in the mushy zone near the end of solidification, therefore a so-called ‘simplified porosity model’ is introduced [14, 15]. When the temperature drops below the critical temperature of T_{cr}, volume shrinkage by solidification is ignored, i.e. the solidification is assumed to occur without volume change. This treatment is made by assuming that the rest melt deep in the mushy zone solidifies as a solid-pore mixture with the mixture density equal to the liquid density.

2. SIMULATION SETTINGS

A 2.45 ton ingot was preliminarily simulated in full 3D (average mesh size of 10 mm) and 2D (average mesh size of 5 mm). The ingot had a square cross-section; however, for the 2D calculation an axis-symmetry is assumed. Casting conditions, process parameters, experimentally measured macrosegregation and shrinkage cavity information were reported previously [16, 17]. The alloy is multi-componential but currently we consider a simplified binary alloy (Fe-0.45

INDEX

wt.%C). The material properties and some important boundary conditions are summarized in Table 2 and Fig. 2. No mould filling is calculated, and the mould is assumed to be initially filled with liquid melt of 1770 K (above liquidus of 1768.95 K). As solidification starts, the casting shrinks and it sucks the gas phase (air) from the top 'pressure inlet'. A zero-gradient boundary condition is applied at the 'pressure inlet' for the other quantities: temperature, concentrations, equiaxed number density. No radiation heat transfer from the top to the ambience is accounted for. Nucleation parameters of equiaxed crystals are: n_{max} = 5.0 x 10^{-3} m^{-3}, ΔT_N = 5.0 K, ΔT_σ = 2.0 K. Calculation with the 4-phase model including air as gas phase is extremely time consuming (demanding tiny small time step), especially when a 3D calculation is performed. The situation can be significantly improved by considering a covering liquid slag instead of gas phase.

Table 2. Thermodynamic & physical properties

Steel		
melting point of pure iron, T_f	K	1805.15
liquidus slope, m	K (wt.%)$^{-1}$	-80.45
equilibrium partition coefficient, k	-	0.36
melt density, ρ_ℓ	kg/m^3	6990
solid density, ρ_e , ρ_c	kg/m^3	7140
specific heat, c_p^ℓ , c_p^c , c_p^e	J/kg/K	500
thermal conductivity, k_ℓ , k_e , k_c	W/m/K	34.0
latent heat, L	J/kg	2.71 × 10^5
viscosity, μ_ℓ	kg/m/s	4.2 × 10^{-3}
thermal expansion coefficient, β_T	K^{-1}	1.07 × 10^{-4}
solutal expansion coefficient, β_c	wt.%$^{-1}$	1.4 × 10^{-2}
dendritic arm spacing, λ_1	M	5 × 10^{-4}
diffusion coefficient (liquid), D_ℓ	m^2/s	2.0 × 10^{-8}
diffusion coefficient (solid), D_e , D_c	m^2/s	1.0 × 10^{-9}
Covering slag		
viscosity, μ_{slag}	kg/m/s	0.01
density, ρ_{slag}	kg/m^3	2500
specific heat, c_{slag}^g	J/kg/K	1815
thermal conductivity, k_{slag}	W/m/K	4.0

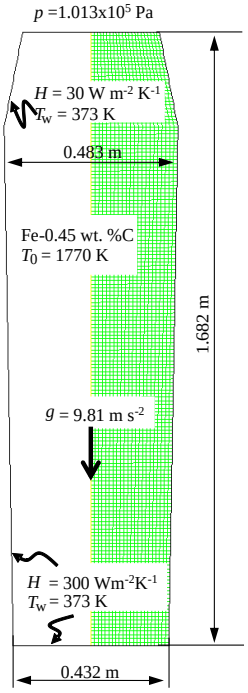

Figure 2. Configuration of the 2.45-ton industrial steel ingot.

3. RESULTS AND DISCUSSION

Example of the solidification sequence at 600 s is shown in Fig. 3. The overall solidification process is mainly governed by heat transfer. The cooling and solidification starts from the mould wall. The columnar phase develops from the mould wall and grows towards the casting centre. In the meantime equiaxed grains nucleate and grow in front of the columnar tips, and those equiaxed grains start to sink and try to settle in the bottom region. The melt is dragged downwards along the columnar tip front by the sinking grains, which in turn induces a rising melt flow in the middle of the ingot. Thermal-solutal convection contributes as well to the interdendritic flow and global melt flow in the bulk. Both $\bar{u}_\ell$ and $\bar{u}_e$ fields are naturally instable. As the flow field of the melt and the motion of the equiaxed grains are fully coupled with other transport phenomena (energy, species and mass), the instability of the flow patterns will directly influence the solidification sequence. Sedimentation of crystals at the bottom region causes the volume fraction of the equiaxed phase to reach a quite high level. When f_e in the lower part of the ingot is high enough (larger than the so-called mechanical blocking limit of 0.49, Fig. 3(b)), the columnar-to-equiaxed transition (CET) occurs.

INDEX

In the upper part of the ingot the columnar tips can continue to grow as the amount of equiaxed crystals is too low to cause blocking. Flow and crystal sedimentation are key mechanisms for the formation of macrosegregation in ingot casting, and they were discussed previously [9, 10, 17]. The final segregation result is shown in Fig. 4. A conically shaped negative segregation zone is found at the bottom region, which coincides with the equiaxed sedimentation zone. A large positive segregated area just below the top shrinkage cavity is predicted. Interestingly, segregation pattern in the lower part of the ingot is quite non-symmetry and non-uniform. Some local positive segregation spots on the casting surface and even inside the cross section are found. Most possible reason for this might be the unstable flow and motion of crystals during the early stage of solidification. Note that the long calculation time (2 weeks in cluster with 12 cores of 3.5 GHz) does not allow performing parameter study in 3D. Another reason for the segregation spots can be possible numerical inaccuracies, which demands further investigation. The segregation pattern in the upper part is much more uniformly distributed on the surface and in the cross section.

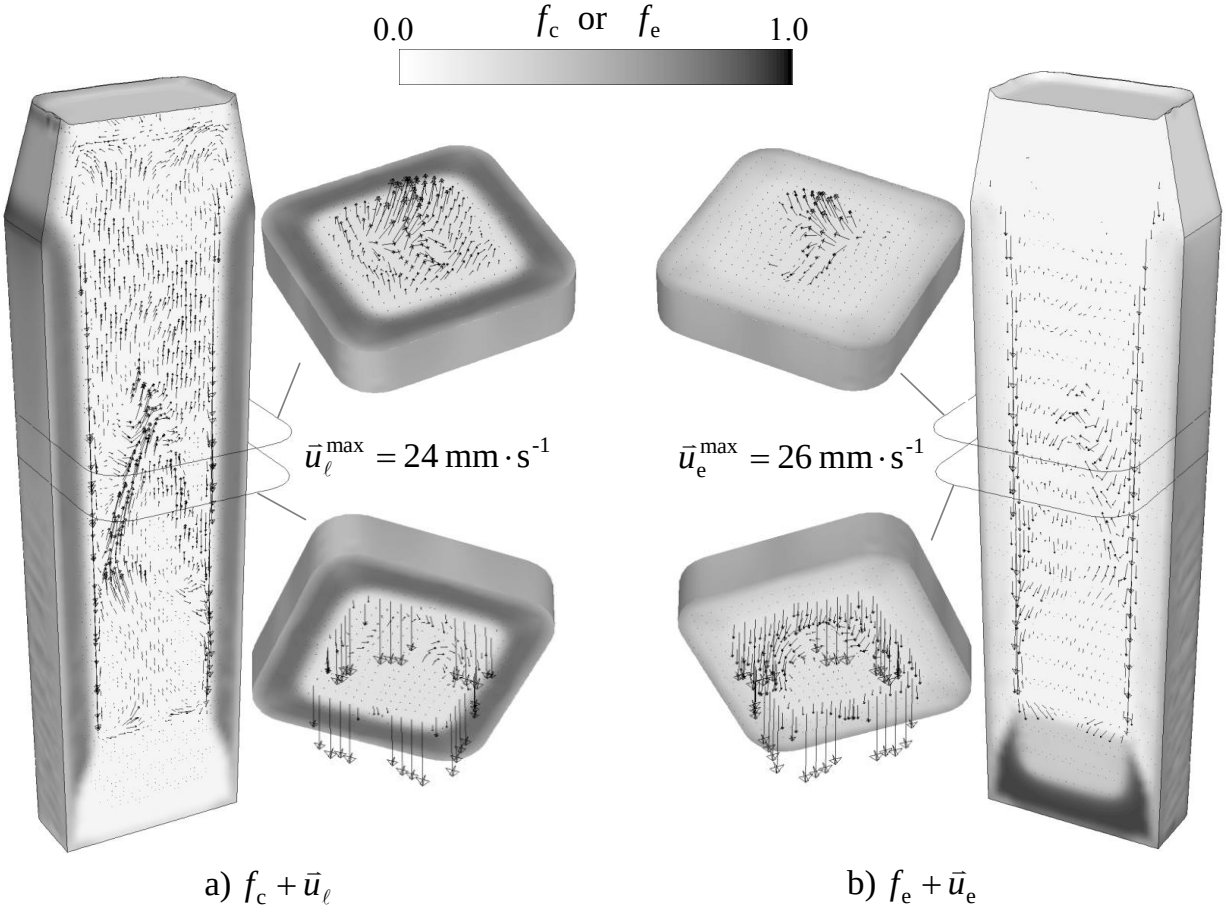

Figure 3. Solidification sequence at 600 s. Both f_c and f_e in the centre vertical section are shown in grey scale with light for lower and dark for high volume fraction. a) The velocity of the melt, $\vec{u}_\ell$ is shown together with f_c, b) while the velocity of the equiaxed crystals, $\vec{u}_e$ is with f_e. Additionally, the phase distributions and velocity fields in 2 horizontal sections are also shown.

The formation of the shrinkage cavity is shown in Fig. 5. The free surface, i.e. the interface between the liquid slag and metal phase, is represented by the iso-surface of f_g = 0.5 with 'g' standing for the slag phase. The numerical thickness of the interface is confined in 2~3 neighbouring elements. With progressing solidification, the forming cavity is continuously filled by the slag from the inlet. The final volume of the cavity is predicted to be 0.00725 m^3, i.e. 2.15% of the volume of the entire ingot (V_0 = 0.3362

INDEX

m^3), which agrees with the solidification shrinkage of the alloy, $\beta = 2.1\%$. The formation of the microscopic shrinkage porosity is calculated indirectly by the CBN criterion, based on the thermal field as post-processing. The final distribution of the CBN value is shown in Fig. 6. The smallest CBN value is located in the middle of the casting centreline, indicating the most possible position with the highest amount of shrinkage pores there.

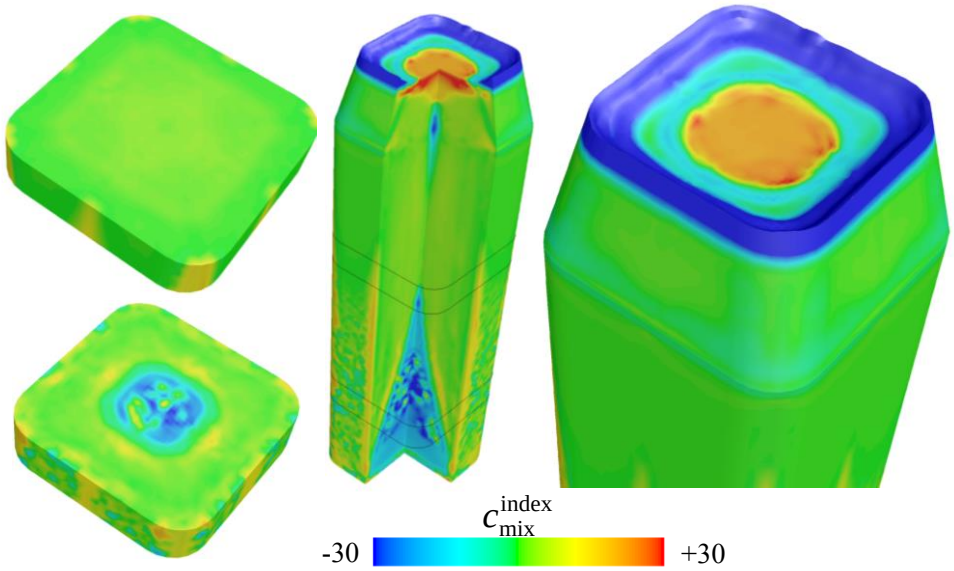

Figure 4. Final segregation distribution. The segregation index, $c_{mix}^{index}=100\times(c_{mix}-c_0)/c_0$, is used to evaluate the macrosegregation, where c_{mix} is the local mixture concentration of the metal phases (equiaxed, columnar and rest eutectic).

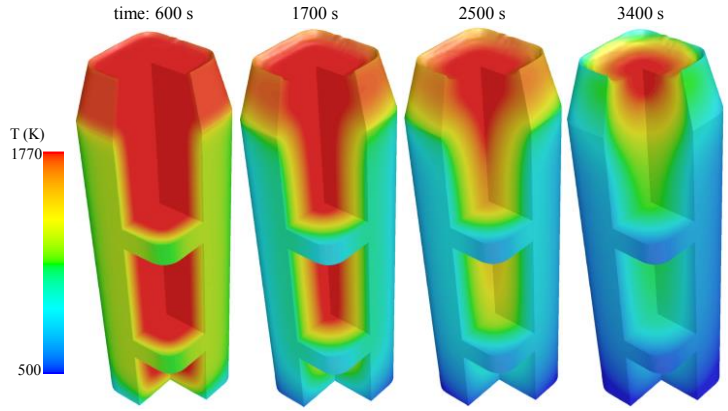

Figure 5. Cavity formation sequence at the hot top. Temperature field is shown in colour.

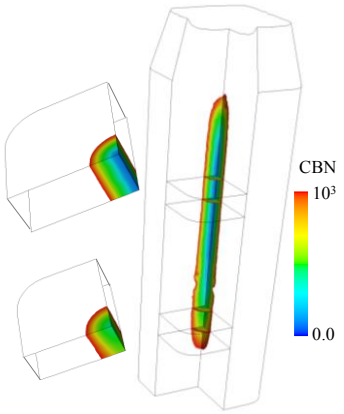

Figure 6. CBN criterion for microscopic shrinkage porosity.

The same casting was also calculated in 2D axis symmetry (but with an average mesh size of half of that used for 3D). The solidification sequence, the shrinkage cavity and CBN criterion of the 2D result are quite similar to those of 3D. And the global macrosegregation pattern is also predicted similar: the conic-negative segregation in the equiaxed sedimentation zone and the large positive segregation below the top shrinkage cavity. The major difference is that quasi-A-segregations [8, 9] in the middle radius region of the ingot are predicted by the 2D calculation, which are not clearly visible for the 3D calculation. One reason is the grid resolution, as being studied previously [17].

INDEX

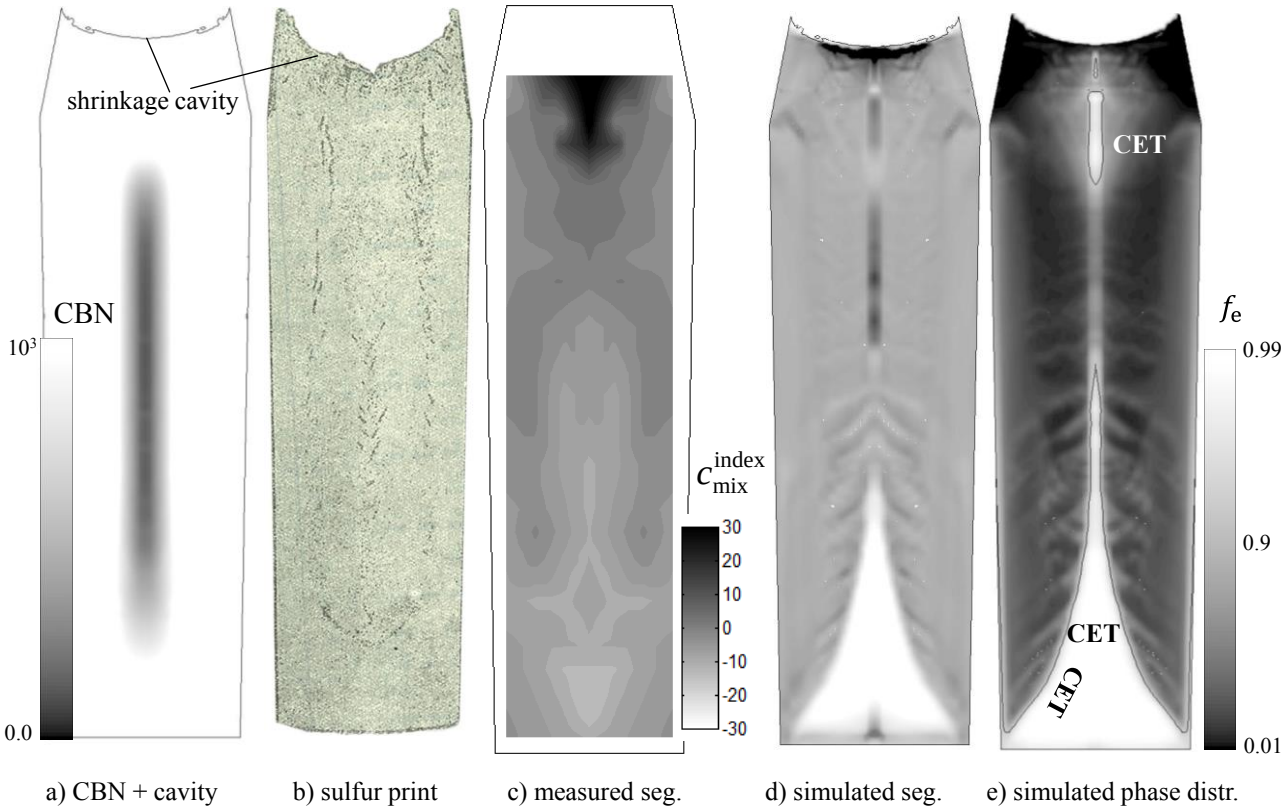

Figure 7. Comparison of the numerical simulation (2D axis symmetry with grid size of 5 mm) with experiments as reported in [16]. a) numerical prediction of the shrinkage cavity and position of the microscopic shrinkage porosity by the CBN criterion; b) sulphur print; c) reconstructed segregation map in grey scale (chemical analysis of 54 drilling samples); d) predicted segregation map in grey scale; e) phase distribution of f_e and marked CET line.

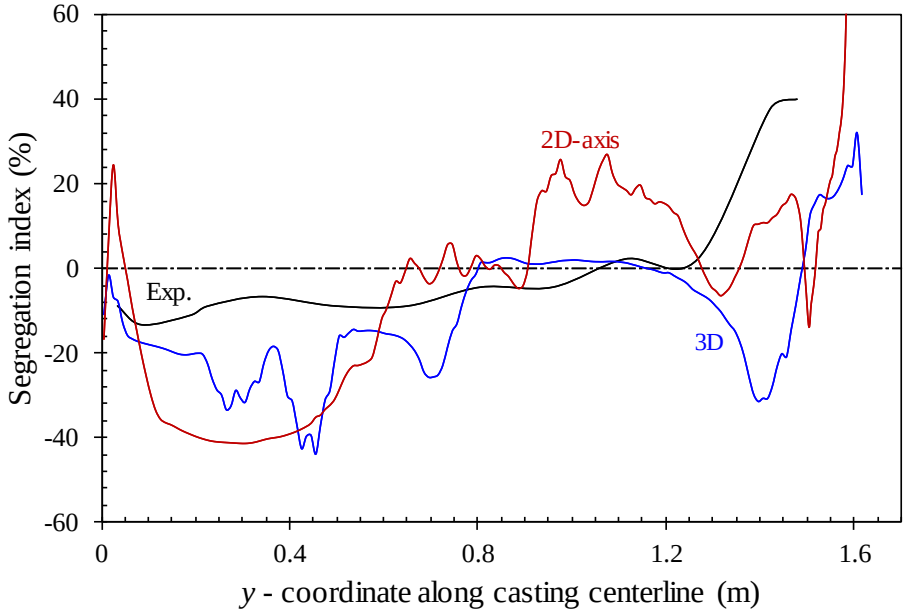

Figure 8. Comparison of centreline segregation (c_{mix}^{index}) between simulations (2D and 3D) and experimental results.

INDEX

Another reason might be due to the dimensions of the geometry. Although the 3D calculation predicts the instable flow (fluctuation) pattern in the bulk region during solidification, the 2D calculation ignoring the swirl flow in the third dimension would exaggerate instability of the flow in the considered 2 dimensions, and exaggerate the initiation and growth of channels. The quasi-A-segregations are an indicator (although not finally proved yet) of the formation of channel segregations. The final macrosegregation pattern, and phase distribution, and the predicted shrinkage cavity and CBN criterion are shown in Fig. 7. They show some similarity to experimental results.

A similar profile of shrinkage cavity is predicted, but the volume of the cavity is smaller than that of the experiment. The negative segregation in the sedimentation zone is overestimated by the simulation. The middle-radius segregation is also partially evidenced by the sulphur print, but it seems not as strong as the simulation shows. The macrosegregation along the casting centreline is also plotted and compared with experimental results (Fig. 8). Both 2D and 3D calculations have predicted some similar variation features of macrosegregation along the centreline, but the quantitative deviation from the experimental result is still quite large.

4. CONCLUSION

The calculation of a 2.45 ton ingot has demonstrated the functionalities of the newly proposed 4-phase model. The goal to use an Eulerian volume averaging approach to model the as-cast columnar-equiaxed structure including CET (columnar-to-equiaxed transition), shrinkage cavity/porosity, and macrosegregation at the process scale for industrial castings seems to be achievable. The highest significance of the model lies in the consideration of the interaction between the solidification shrinkage and the formation of macrosegregation.

The current model is an extension of the previous mixed columnar-equiaxed solidification model [10] by considering an additional gas (or covering liquid slag) phase. The new phase is supposed to be immiscible with other phases. It has no mass and species transfer with other phases, but the treatment of momentum and enthalpy exchanges with other phases becomes crucially important to get a sharp interface between the liquid slag and other metal phases. Both 3D and 2D calculations show that the thickness of the interface between the slag and metal phases is confined in the 2~3 neighbouring elements. It means that the refinement of grid size improves the sharpness of the interface. It is here verified that the shrinkage cavity can be dealt with Eulerian approach. The volume of the formed cavity in the hot top coincides well with the total volume shrinkage by solidification of the ingot.

The implemented CBN criterion is a further indicator for the possible occurrence of microscopic porosity. As the reported experimental data of this ingot [16] is not sufficient to verify the microscopic shrinkage result, no comment can be made here. However, many valuable works were done by other researchers [2, 3].

A few points about the current macrosegregation model and modelling results must be mentioned. Although the key segregation features of industry ingot can be ‘reproduced’ numerically, the quantitative severity of macrosegregation is predicted significantly discrepant from the reality. As we have investigated previously [9, 17], the main reasons are (i) the ignored dendritic morphology which exaggerates sedimentation induced negative segregation at the bottom; (ii) the grid size which is still too large to resolve the possible channel segregates; (iii) the shortage of adequate process parameters and materials properties; (iv) the simplification of multicomponent alloy system with a binary alloy. Finally, it has to be mentioned that the calculation cost increases intensively with an increase of the number of phases.

ACKNOWLEDGEMENT

This work was financially supported by the FWF Austrian Science Fund (P23155-N24), FFG Bridge Early Stage (No. 842441), and the Austrian Federal Ministry of Economy, Family and Youth and the National Foundation for Research, Technology and Development within the framework of the Christian Doppler Laboratory for Advanced Process Simulation of Solidification and Melting.

INDEX

REFERENCES

[1] Moore J. and Shah N.: Int. Metals Rev., 28 (1983), p. 338-356.
[2] Niyama E., Uchida T., Morikawa M. and Saito S.: AFS Cast Met. Res. J., 7 (1982), p. 52-63.
[3] Carlson K. D., and Beckermann C.: Metall. Mater. Trans., 40A (2009), p. 163-175.
[4] Nastac L. and Marsden K.: Int. J. Cast Metal Res., 26 (2013), p. 374-382.
[5] Wu M., Schädlich-Stubenrauch J., Augthun M., Sahm P. and Spiekermann H.: Dent. Mater., 14 (1998), p. 321-328.
[6] Ludwig A., Gruber-Pretzler M., Mayer F., Ishmurzin A. and Wu M.: Mater. Sci. Eng. A, 413-414 (2005), p. 485-489.
[7] Wu M., Könözsy L., Ludwig A., Schützenhöfer W. and Tanzer R.: Steel Res. Int., 79 (2008), p. 637-644.
[8] Wu M., Li J., Ludwig A. and Kharicha A.: Comp. Mater. Sci., 79 (2013), p. 830-840.
[9] Wu M., Li J., Ludwig A. and Kharicha A.: Comp. Mater. Sci., 92 (2014), p. 267-285.
[10] Wu M. and Ludwig A.: Metall. Mater. Trans., 37A (2006), p.1613-1624.
[11] Wang T., Yao S., Zhang X., Jin J., Wu M., Ludwig A., Pustal B. and Bührig-Polaczek A.: Jinshu Xuebao/Acta Metall. Sinica, 42 (2006), p.584-590.
[12] Ranz W. and Marshall W.: Chem. Eng. Prog., 48 (1952), p.141-146.
[13] ANSYS FLUENT 12.0 User's Guide, Copyright © 2009 by ANSYS, Inc, April 2009.
[14] Mayer F., Wu M. and Ludwig A.: Steel Res. Int., 81 (2010), p. 660-667.
[15] Wu M., Domitner J. and Ludwig A.: Metall. Mater. Trans. A, 43 (2012), p. 945-963.
[16] Iron Steel Inst.: Report on the heterogeneity of steel ingots, J. Iron Steel Inst., 103 (1926), p.39-151.
[17] Li J., Wu M., Kharicha A. and Ludwig A.: Int. J. Heat and Mass Transfer, 72 (2014), p. 668-679.

INDEX